

RESEARCH ARTICLE | FEBRUARY 12 2025

Computational screening of complex oxides for next-generation thermal barrier coatings






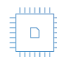
Majid Zeraati ; Artem R. Oganov ; Alexey P. Maltsev ; Sergey F. Solodovnikov 



J. Appl. Phys. 137, 065106 (2025)


<https://doi.org/10.1063/5.0253010>



 Nanotechnology & Materials Science  Optics & Photonics  Impedance Analysis  Scanning Probe Microscopy  Sensors  Failure Analysis & Semiconductors

Unlock the Full Spectrum.
From DC to 8.5 GHz.
Your Application. Measured.

[Find out more](#)



Computational screening of complex oxides for next-generation thermal barrier coatings

Cite as: J. Appl. Phys. 137, 065106 (2025); doi: 10.1063/5.0253010

Submitted: 13 December 2024 · Accepted: 17 January 2025 ·

Published Online: 12 February 2025



Majid Zeraati,^{1,a)} Artem R. Oganov,¹ Alexey P. Maltsev,¹ and Sergey F. Solodovnikov²

AFFILIATIONS

¹Skolkovo Institute of Science and Technology, Bolshoy Boulevard 30, Bld. 1, Moscow 121205, Russia

²Nikolaev Institute of Inorganic Chemistry, Siberian Branch, Russian Academy of Sciences, Academician Lavrentiev Ave. 3, Novosibirsk 630090, Russia

^{a)}Author to whom correspondence should be addressed: Majid.Zeraati@skoltech.ru

ABSTRACT

Thermal barrier coatings are crucial for industries like aerospace and energy that rely on high temperatures, shielding metal, ceramic, or composite components from heat damage. Ytria-stabilized zirconia is one of the best thermal barrier coating (TBC) material due to its high-temperature stability and oxidation resistance, but it has drawbacks such as thermal phase transition at 1150–1200 °C and high oxygen conductivity limit the number of thermal cycles and operating temperature at 1200 °C. Thus, it is essential to find new TBC materials with low thermal conductivity, high thermal expansion coefficient, high phase, and thermal, mechanical, and chemical stability under oxidizing conditions to enhance performance and efficiency. In this study, using advanced computational methods, including AI and molecular dynamics simulations, we proposed several promising complex oxides with suitable structures, thermal and mechanical properties that could be further studied experimentally as TBC materials. Having calculated thermophysical properties of complex oxides with structures of perovskite, pyrochlore, garnet, and their derivatives. Using rigorous criteria, we have identified 14 new compounds with potential TBC applications. Overall, this research highlights the importance of computational techniques in material discovery for TBC applications.

© 2025 Author(s). All article content, except where otherwise noted, is licensed under a Creative Commons Attribution-NonCommercial 4.0 International (CC BY-NC) license (<https://creativecommons.org/licenses/by-nc/4.0/>). <https://doi.org/10.1063/5.0253010>

I. INTRODUCTION

Thermal barrier coatings (TBCs) are vital components in the aerospace, energy, and high-temperature-related industries. Serving as protective layers on the surfaces of components made of metals, ceramics, or composites, these coatings prevent damages caused by high temperatures and heat transfer to other parts of the system.^{1–3} With the increasing demand for performance and durability in high-temperature conditions, the importance of developing and optimizing thermal barrier coatings has grown significantly.

Currently, the main material used for TBCs is yttria-stabilized zirconia (YSZ),¹ due to its stability at high temperatures, oxidation, erosion and corrosion resistance, and desirable thermophysical properties. The disadvantages of these coatings include phase transition at 1150–1200 °C and high oxygen conductivity limiting the number of thermal cycles and operating temperature at 1200 °C for YSZ.

Finding new materials for TBCs is crucial. New materials with features such as low heat transfer capability, suitably high thermal expansion coefficient (TEC), high phase, and thermal, mechanical, and chemical stability in dusty air could improve the performance and efficiency of these coatings. Additionally, developing materials with lower weight and better thermophysical properties can reduce the overall weight of gas turbines and enhance the efficiency and application of thermal coatings. These materials can also provide higher resistance to mechanical damage from impact, pressure, and vibrations, leading to a decrease in failures and an increase in the useful life of components. Furthermore, considering different environmental conditions, new materials with greater resistance to oxidation can extend the useful life of the coating. Therefore, research and development in finding new materials for thermal barrier coatings are of great importance and can contribute to improving the performance and durability of systems utilizing these coatings.

02 March 2025 13:03:23

The initial base for selecting the trial oxide compounds for our work is crystal chemistry considerations following from high thermal stability, TEC, mechanical strength, and low thermal conductivity of the materials for TBCs. These requirements point to complex oxides, which combine alternating hard and soft structural units³ with corresponding strong and weak chemical bonds in coordination polyhedra of small and highly charged cations B with constant oxidation state B (Al^{3+} , Zr^{4+} , Nb^{5+} , etc.) and large cations A (alkaline earth or rare earth ions). These polyhedra should be linked into flexible, extended, and highly symmetric structures, which ensures its strength, thermal stability, and relatively high TEC.

In our previous study,⁴ using theoretical calculations taking advantage of the machine-learning interatomic potentials, we studied more than 30 cubic, hexagonal, tetragonal, and orthorhombic complex oxides with framework and layered structures, and we were able to suggest several compounds with thermophysical properties suitable for TBC materials. In this study, we intend to continue our work on calculating thermophysical properties of selected complex oxides, focusing on the cubic framework structures of perovskite ABO_3 , pyrochlore $\text{A}_2\text{B}_2\text{O}_7$, garnet $\text{A}_3\text{B}_2\text{C}_3\text{O}_{12}$, and their derivatives, which are of greatest interest in terms of increasing the strength of the structure, the isotropy of the TEC, and other properties of TBCs.

II. METHODS

Our study employed molecular dynamics (MD) simulations to determine thermal conductivity and TEC. For these calculations, 20 known compounds of the perovskite, pyrochlore, garnet types, and their derivatives were selected. In addition, nine hypothetical compounds with perovskite- or pyrochlore-like structures and three known compounds with the same supposed structures were taken. For all structures, the optimizations at each temperature were automatically obtained through MD simulations. The phase transitions in perovskite-like SrHfO_3 and CaZrO_3 were investigated too. For these materials, the thermal conductivity of the corresponding stable phases at different temperatures were calculated. For $\text{Sr}_2\text{AlNbO}_6$, we studied two alternative cubic structures of the double perovskite type and the disordered perovskite type. For all other compounds, only the ordered structures were considered.

Despite its computational cost, achieving high accuracy in MD simulations typically involves employing density functional theory (DFT). An alternative to DFT is the utilization of machine-learning interatomic potentials (MLPs), which offer comparable accuracy to DFT but at a significantly reduced computational cost. In many studies, the capability and reliability of MLPs in calculating thermal conductivity have been evaluated, and their usage has been established as a trusted method.⁴⁻⁸

A. Machine-learning potentials

We used *ab initio* molecular dynamics (AIMD) as implemented in the VASP code,⁹ with projector-augmented wave (PAW)¹⁰ potentials and the PBEsol and PBE exchange-correlation functionals.^{11,12} All AIMD calculations were performed on different supercells and *k*-point grids¹³ using the *NPT* ensemble.^{14,15} The total simulation time for AIMD runs was 20 ps with a time step of

2 fs. During AIMD simulations, we gradually increased the temperature from 0 to 2300 K.

We prepared the initial training set by selecting 500 random configurations from AIMD and proceeded with the initial training of moment tensor potentials (MTPs)¹⁶⁻¹⁹ with a cutoff radius $r_c = 5 \text{ \AA}$. After this initial step, we employed the D-optimality-based active learning method to further train the MTP, as implemented in the MLIP package.²⁰ Using the obtained initial potential, we performed classical MD simulations with the *NPT* ensemble gradually from 0 to 2300 K for 100 ps. Throughout this simulation, we selected new configurations using the active learning method. The energy, forces, and stresses of these new configurations were calculated using DFT. Subsequently, the MTP potentials were retrained using the new training sets. This entire process was repeated until no new configurations were selected using the active learning approach. For classical MD simulations, we used the large-scale atomic/molecular massively parallel simulator (LAMMPS) package,²¹ interfaced with the MLIP code.

To perform long MD simulation in the large simulation boxes, we employed new neuroevolution potentials (NEPs)²²⁻²⁵ which is implemented in the GPUMD package.²⁶ These NEPs were trained using the same training sets with MTP. The cutoff radii for radial and angular descriptor parts in NEP are $r_c^R = 6 \text{ \AA}$ and $r_c^A = 6 \text{ \AA}$, respectively. The errors in energy and forces for each type of potential and other properties are presented in Table I.

B. Thermal expansion coefficient

Understanding the TECs is important for TBCs due to their application in high-temperature environments, such as gas turbine engines. TBCs act as insulating layers and protect the underlying components from extreme heat. However, during operation, these components experience significant temperature fluctuations that result in thermal expansion and contraction. Volumetric TEC determines the amount of expansion or contraction of a material with temperature changes [see Eq. (1)], which is critical to ensure the integrity and durability of TBCs under thermal cycling conditions. Detailed knowledge of TEC helps engineers design TBCs with appropriate thermal mismatch properties, prevent flaking and cracking, and ultimately increase the performance and lifetime of coated components in harsh environments. Volumetric TEC was calculated as

$$\alpha_v = \frac{1}{V} \frac{dV}{dT}. \quad (1)$$

There are various methods to calculate the theoretical TEC such as quasi-harmonic approximation (QHA) and MD simulation.²⁷⁻²⁹ QHA can predict TEC with good accuracy at lower than Debye temperatures, but at high temperatures, it overestimates the value of TEC. MD simulation correctly predicts TEC at high temperatures due to the classical nature of the method (but note that we are mostly interested in high-temperature properties here).

MD simulation can include all anharmonicity which is essential to predict TEC for TBCs at high temperatures, but at low temperatures, it needs quantum correction to calculate TEC. One of the effective computational technique to do this is path-integral molecular dynamics (PIMD) simulation.³⁰

TABLE I. The errors in energy and forces for each type of potential and supercell size in MD simulation boxes, along with the number of atoms in each box, were calculated for TEC and thermal conductivity.

Compound (structure)	MTP error (RMSE)		NEP error (RMSE)		MD simulation box	
	Energy/N (meV)	Forces (meV/Å)	Energy/N (meV)	Forces (meV/Å)	Supercell	N atoms
Sr ₂ AlNbO ₆ (double perovskite)	1.23	46.78	1.08	51.69	10 × 10 × 10	40 000
BaHfO ₃ (cubic perovskite)	1.32	52.99	0.90	40.42	20 × 20 × 20	40 000
Sr ₂ AlNbO ₆ (disordered double perovskite)	1.34	50.26	1.20	56.39	10 × 10 × 10	40 000
Sr ₂ AlTaO ₆ (double perovskite)	1.95	56.25	1.76	52.06	10 × 10 × 10	40 000
SrTiO ₃ (cubic perovskite)	3.11	56.89	2.36	66.26	20 × 20 × 20	40 000
SrHfO ₃ (perovskite, GdFeO ₃ type)	1.37	54.01	1.05	43.95	20 × 20 × 20	40 000
Y ₂ Ti ₂ O ₇ (cubic pyrochlore)	2.18	130.21	1.41	103.72	8 × 8 × 8	45 056
CaZrO ₃ (perovskite, GdFeO ₃ type)	1.76	69.90	1.36	58.61	20 × 20 × 20	40 000
Gd ₃ Sc ₂ Al ₃ O ₁₂ (garnet)	0.54	47.44	0.47	50.85	8 × 8 × 8	81 920
Ca ₂ LaHf ₂ Al ₃ O ₁₂ (garnet)	0.94	95.08	0.69	67.25	6 × 6 × 6	34 560
SrBa ₂ MgTa ₂ O ₉ ^{a,b} (trigonal double perovskite)	1.38	110.97	0.92	78.03	14 × 14 × 12	35 280
Ba ₃ MgTa ₂ O ₉ ^a (trigonal double perovskite)	1.42	95.50	1.08	81.37	12 × 12 × 10	21 600
Ba ₃ YHfTaO ₉ ^{a,b} (trigonal double perovskite)	1.26	104.90	1.01	75.07	14 × 14 × 12	35 280
SrBa ₂ MgNb ₂ O ₉ ^{a,b} (trigonal double perovskite)	1.63	116.74	1.07	86.79	14 × 14 × 12	35 280
Gd ₂ Ti ₂ O ₇ (cubic pyrochlore)	7.88	106.88	1.49	98.95	8 × 8 × 8	45 056
La ₃ Lu ₂ Ga ₃ O ₁₂ (garnet)	0.81	64.90	0.67	63.25	8 × 8 × 8	81 920
Ba ₃ YZrTaO ₉ ^{a,b} (trigonal double perovskite)	1.37	108.47	1.11	75.83	14 × 14 × 12	35 280
Ba ₃ YTiTaO ₉ ^{a,c} (trigonal double perovskite)	1.31	82.57	1.18	80.16	14 × 14 × 12	35 280
Y ₂ AlTaO ₇ ^{a,b} (weberite)	3.47	172.47	3.14	134.15	12 × 12 × 5	47 520
La ₃ Ca ₂ Nb ₃ O ₁₄ ^a (trigonal ordered pyrochlore)	3.76	177.44	1.34	122.03	12 × 12 × 5	47 520
Ba ₃ YHfNbO ₉ ^{a,b} (trigonal double perovskite)	1.40	109.37	1.07	72.79	14 × 14 × 12	35 280
Sr ₃ Y ₂ Ge ₃ O ₁₂ (garnet)	0.09	87.96	0.68	62.53	6 × 6 × 6	34 560
Ba ₃ YZrNbO ₉ ^{a,b} (trigonal double perovskite)	1.47	115.43	1.14	78.54	14 × 14 × 12	35 280
La ₃ Mg ₂ Ta ₃ O ₁₄ ^{a,c} (trigonal ordered pyrochlore)	2.01	142.86	0.92	99.40	12 × 12 × 5	47 520
La ₃ Mg ₂ Nb ₃ O ₁₄ ^{a,b} (trigonal ordered pyrochlore)	2.50	163.82	1.26	121.25	12 × 12 × 5	47 520
La ₃ Ca ₂ Ta ₃ O ₁₄ ^{a,b} (trigonal ordered pyrochlore)	1.95	145.64	1.05	103.17	12 × 12 × 5	47 520
Y ₃ Ca ₂ Nb ₃ O ₁₄ ^{a,b} (trigonal pyrochlore)	3.40	175.80	1.89	122.24	12 × 12 × 5	47 520
Gd ₂ AlTaO ₇ ^{a,c} (weberite)	3.67	154.32	1.80	118.63	12 × 12 × 5	47 520
Gd ₂ Zr ₂ O ₇ (cubic pyrochlore)	1.43	81.68	1.28	84.76	8 × 8 × 8	45 056
Gd ₃ Ga ₅ O ₁₂ (garnet)	0.69	68.38	0.51	49.33	6 × 6 × 6	34 560
Ca ₃ Y ₂ Ge ₃ O ₁₂ (garnet)	1.06	88.90	0.72	63.57	6 × 6 × 6	34 560
La ₃ TaO ₇ ^a (distorted weberite)	2.23	148.86	1.10	110.25	12 × 12 × 8	50 688
Gd ₃ Sc ₂ Ga ₃ O ₁₂ (garnet)	2.01	144.11	1.54	106.10	6 × 6 × 6	34 560
Gd ₂ Hf ₂ O ₇ (cubic pyrochlore)	4.48	72.43	1.14	73.40	8 × 8 × 8	45 056

^aMaterials with the anisotropic structure.^bHypothetical compounds.^cKnown compounds and hypothetical compounds.

This method accounts for quantum-mechanical effects in nuclear motion, which is essential for predicting TEC at low temperatures. PIMD is a method based on the quantum mechanical path-integral formulation, initially developed by Feynman and Hibbs³¹ and later implemented in molecular dynamics by Parrinello and Rahman.³² PIMD allows the simulation of quantum effects at finite temperatures by representing each quantum particle as a “ring polymer” consisting of P replicas, or “beads,” connected by harmonic springs.³⁰ This effectively maps the quantum partition function onto a classical one. This mapping enables a classical simulation of quantum-

mechanical systems. More information about implementation of PIMD in GPUMD package is available in Ref. 33.

C. Thermal conductivity

Calculating the thermal conductivity of TBC materials is challenging. TBC materials are insulators, and their thermal conductivity is primarily dominated by phonons (lattice thermal conductivity). Due to the complex structures and strongly anharmonicity in TBC materials, calculating their thermal conductivity at high temperatures is not

02 March 2025 13:03:23

straightforward. Experiments have shown that thermal conductivity of most TBCs at high temperatures exhibits weak dependence on temperature.^{34–36} However, most phonon gas models, such as the Boltzmann transport equation (BTE),^{37–39} predict thermal conductivity $\kappa \propto T^{-1}$.

In our previous study,⁴ we compared several theoretical methods for calculating lattice thermal conductivity, such as the BTE, effective harmonic model (EHM),^{40–42} and homogeneous nonequilibrium molecular dynamics (HNEMD),^{43–45} with available experimental data of thermal conductivity for $\text{La}_2\text{Zr}_2\text{O}_7$, ZrSiO_4 , and BaZrO_3 across a wide range of temperatures. In that study, we found that solving the BTE only with temperature-dependent interatomic force constants (TDIFCs) and HNEMD, which considers the anharmonic nature of atomic vibrations, gives reliable values of thermal conductivity for TBCs at high temperatures. Therefore, in this study, we will utilize HNEMD due to its reliability and applicability under all conditions, from crystalline to amorphous, to calculate thermal conductivity.

All the HNEMD simulations were performed in the Nose-Hoover chain thermostat^{43,44} to achieve the convergence of the κ value using GPUMD package.

Note that classical MD simulations follow the classical Boltzmann statistics. However, at temperatures below the Debye temperature, quantum Bose-Einstein vibrational statistics become crucial. Therefore, it is essential to utilize a quantum-correction method to correct the thermal conductivity at low temperatures. In HNEMD simulation, the classical spectral thermal conductivity is then derived as

$$\kappa(\omega, T) = \frac{2}{VTF_e} \int_0^\infty dt e^{i\omega t} K(t). \quad (2)$$

Here, V is the volume of simulation box, T is the temperature, and F_e is the external driving force.

With the classical spectral thermal conductivity available, the quantum-corrected spectral thermal conductivity $\kappa^q(\omega, T)$ can be derived by multiplying $\kappa(\omega, T)$ with the probability $p(x)$ between the quantum and classical modal heat capacity,^{46–49}

$$\kappa^q(\omega, T) = \kappa(\omega, T)p(x), \quad (3)$$

where

$$p(x) = \frac{x^2 e^x}{(e^x - 1)^2}. \quad (4)$$

In these equations, $x = \hbar\omega/k_B T$, where \hbar represents the reduced Planck constant and k_B denotes the Boltzmann constant. The total quantum-corrected thermal conductivity can be rewritten as

$$\kappa^q(T) = \int_0^\infty \frac{d\omega}{2\pi} \kappa^q(\omega, T). \quad (5)$$

D. Elastic constants and mechanical properties

In the homogeneous deformation of a crystal, the relationship between strain and stress is⁵⁰

$$\sigma_{ij} = C_{ijkl}\epsilon_{kl}. \quad (6)$$

Here, σ_{ij} and ϵ_{kl} represent the stress and strain tensors, respectively, while C_{ijkl} denotes the elastic stiffness tensor. For simplified calculations, the stress-strain relationship can be reformulated using the strain energy density function U via the work conjugate relation,⁵¹

$$\sigma_{ij} = \frac{\partial U}{\partial \epsilon_{ij}}. \quad (7)$$

From Eq. (6), it follows that

$$C_{ijkl} = \frac{\partial \sigma_{ij}}{\partial \epsilon_{kl}}. \quad (8)$$

To derive the effective bulk modulus K , shear modulus G , and Young's modulus E , we employed the Voigt-Reuss-Hill averaging schemes.^{52–54}

III. RESULTS AND DISCUSSION

A. Thermal expansion coefficient

We used classical MD and PIMD simulations with the GPUMD package employing NEP potentials to calculate TEC. In our previous study,⁴ we used the ML potentials trained with PBE exchange-correlation functional which tends to overestimate the TEC. In this current study, we used the PBEsol functional, anticipating a more accurate estimation of TEC than with PBE.

To compare the results of the QHA, classical MD, and PIMD methods, we have compared the results obtained for $\text{Ca}_2\text{LaHf}_2\text{Al}_3\text{O}_{12}$ in Fig. 1. The values obtained from classical MD and PIMD are very close to each other at high temperatures, but, the results obtained from QHA are significantly different. On the other hand, at lower temperatures, the results obtained from PIMD and QHA are close to each other.

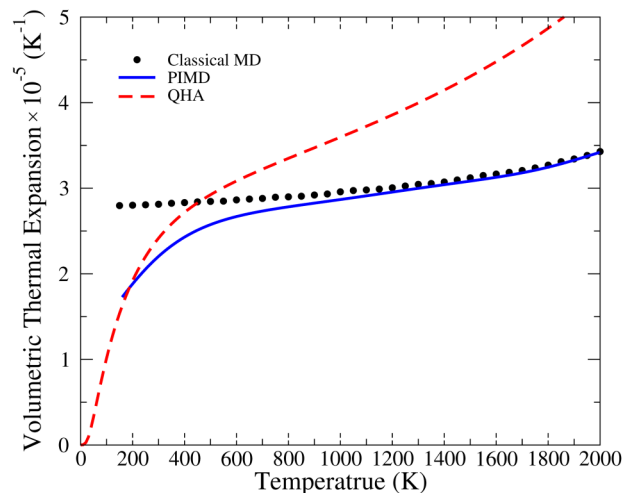


FIG. 1. Volumetric thermal expansion of $\text{Ca}_2\text{LaHf}_2\text{Al}_3\text{O}_{12}$ as a function of temperature calculated using classical MD, QHA, and PIMD.

02 March 2025 13:03:23

Consistent supercell sizes were employed for both thermal conductivity and TEC calculations. Volumetric TECs for each compound at five temperatures ($T = 300, 500, 1000, 1500,$ and 2000 K) are shown in Table II.

The calculated thermal expansion coefficients of the compounds are compared with available experimental data in Table S1 and Fig. S1 in the supplementary material.

For some compounds, such as SrHfO₃ and CaZrO₃, we observed temperature-induced phase transitions. To calculate thermal conductivity of these structures at different temperatures, the stable phase at each temperature was considered. The phase change diagrams for these structures are available in Figs. S2 and S3 in the supplementary material.

B. Thermal conductivity

In order to determine the appropriate value of the external driving force F_e , we performed multiple simulations at 300 K using external forces varying from 10^{-5} to 10^{-4} Å⁻¹. Finally, we selected a value of 5×10^{-5} Å⁻¹ for the driving force. At each temperature, we performed 15 individual simulations at equilibrium volume and calculated the κ value by averaging the results from each simulation.

The calculated values of the thermal conductivity at four different temperatures 300, 1000, 1500, and 2000 K are presented in Table III and Fig. 2. We calculated both classical and quantum-corrected thermal conductivity using the

TABLE II. Thermal expansion coefficients of the compounds calculated using the classical MD and path-integral MD method.

Compound	Volumetric TEC $\times 10^{-5}$ (K ⁻¹)									
	300 K		500 K		1000 K		1500 K		2000 K	
	PIMD	Classical	PIMD	Classical	PIMD	Classical	PIMD	Classical	PIMD	Classical
Sr ₂ AlNbO ₆	2.46	3.09	2.90	3.19	3.44	3.53	3.93	3.95	4.48	4.52
BaHfO ₃	1.96	2.39	2.28	2.47	2.62	2.68	2.91	2.93	3.24	3.27
Sr ₂ AlTaO ₆	2.37	2.91	2.77	2.99	3.21	3.23	3.57	3.55	4.08	3.99
SrTiO ₃	3.69	4.05	3.64	3.83	4.00	3.99	4.39	4.34	4.92	4.82
SrHfO ₃	2.57	3.05	3.04	3.22	3.46	3.53	2.84	2.88	2.90	2.92
Y ₂ Ti ₂ O ₇	3.35	3.91	3.44	3.68	3.43	3.50	3.56	3.58	3.92	3.98
CaZrO ₃	2.52	3.23	2.95	3.32	3.56	3.72	4.16	4.25	4.94	5.73
Gd ₃ Sc ₂ Al ₃ O ₁₂	2.49	3.11	2.92	3.2	3.36	3.42	3.69	3.7	4.14	4.18
Ca ₂ LaHf ₂ Al ₃ O ₁₂	2.20	2.81	2.57	2.84	2.87	2.96	3.08	3.12	3.42	3.43
SrBa ₂ MgTa ₂ O ₉ ^{a,b}	2.73	3.21	3.05	3.26	3.44	3.50	3.82	3.85	4.37	4.48
Ba ₃ MgTa ₂ O ₉ ^a	2.90	3.40	3.28	3.51	3.70	3.79	4.13	4.17	4.63	4.69
Ba ₃ YHfTaO ₉ ^{a,b}	2.11	2.53	2.29	2.46	2.62	2.67	2.95	2.97	3.40	3.41
SrBa ₂ MgNb ₂ O ₉ ^{a,b}	3.02	3.54	3.50	3.58	3.75	3.82	4.20	4.22	4.93	4.93
Gd ₂ Ti ₂ O ₇	3.70	3.96	3.80	4.09	3.95	4.03	4.27	4.28	5.19	5.18
La ₃ Lu ₂ Ga ₃ O ₁₂	2.25	2.61	2.60	2.68	2.97	2.9	3.33	3.21	3.98	3.82
Ba ₃ YZrTaO ₉ ^{a,b}	2.40	2.76	2.37	2.54	2.73	2.77	3.06	3.08	3.48	3.51
Ba ₃ YTiTaO ₉ ^{a,c}	2.44	2.81	2.80	2.96	3.29	3.34	3.80	3.81	4.59	4.58
Y ₂ AlTaO ₇ ^{a,b}	2.36	3.00	2.94	3.21	3.82	3.80	5.94	6.26	5.78	6.12
La ₃ Ca ₂ Nb ₃ O ₁₄ ^a	2.49	2.86	2.94	3.03	3.13	3.15	3.40	3.41	3.99	4.00
Ba ₃ YHfNbO ₉ ^{a,b}	2.61	3.03	2.53	2.71	2.85	2.90	3.19	3.21	3.66	3.67
Sr ₃ Y ₂ Ge ₃ O ₁₂	2.48	3.00	2.86	3.09	3.25	3.31	3.58	3.62	4.14	4.12
Ba ₃ YZrNbO ₉ ^{a,b}	2.48	2.98	2.51	2.68	2.90	2.94	3.29	3.32	3.80	3.81
La ₃ Mg ₂ Ta ₃ O ₁₄ ^{a,c}	2.27	2.94	2.64	3.08	2.97	3.19	3.15	3.40	3.33	4.20
La ₃ Mg ₂ Nb ₃ O ₁₄ ^{a,b}	2.44	2.59	2.75	2.93	3.09	3.13	3.35	3.37	3.95	4.01
La ₃ Ca ₂ Ta ₃ O ₁₄ ^{a,b}	2.46	2.89	2.69	2.90	2.83	2.88	2.97	3.00	3.25	3.27
Y ₃ Ca ₂ Nb ₃ O ₁₄ ^{a,b}	4.94	8.04	2.80	3.96	2.67	2.70	3.25	3.67	6.15	...
Gd ₂ AlTaO ₇ ^{a,c}	2.82	3.30	3.50	3.71	3.75	3.82	4.69	5.29
Gd ₂ Zr ₂ O ₇	3.19	3.72	3.85	4.23	4.23	4.30	3.98	3.99	4.16	4.17
Gd ₃ Ga ₅ O ₁₂	2.69	3.30	3.20	3.45	3.81	3.89	4.43	4.48	5.82	5.89
Ca ₃ Y ₂ Ge ₃ O ₁₂	2.89	3.48	3.25	3.50	3.49	3.56	3.68	3.71	4.02	4.05
La ₃ TaO ₇ ^a	2.88	3.32	3.16	3.33	3.53	3.26	4.11	4.09	5.64	5.49
Gd ₃ Sc ₂ Ga ₃ O ₁₂	2.61	3.22	2.95	3.41	4.72	4.02	7.29	5.32
Gd ₂ Hf ₂ O ₇	3.40	4.33	4.04	4.72	3.21	3.26	3.05	3.07	3.23	3.27

^aMaterials with the anisotropic structure.

^bHypothetical compounds.

^cKnown compounds and hypothetical compounds.

02 March 2025 13:03:23

HNEMD method. As shown in Table III, the difference between classical and quantum-corrected thermal conductivity at above 1000 K is small. However, at low temperatures, such as room temperature, the difference is noticeable. Therefore, it is important to consider the contribution of nuclear quantum effects to thermal conductivity at temperatures below the Debye temperature. This difference between classical and quantum-corrected κ is larger in materials with low thermal conductivity. But still, at high temperatures, this discrepancy is negligible.

The calculated thermal conductivities of the compounds are compared with available experimental data in Table SII and Fig. S4 in the [supplementary material](#).

C. The effect of disorder on thermal conductivity

One key phenomenon to consider when studying thermal conductivity is the impact of disorder. On-site disorder in TBCs significantly affects their thermal conductivity. The introduction of defects leads to increased extrinsic phonon scattering, which

TABLE III. Thermal conductivity of the compounds calculated using the HNEMD method. The compounds are sorted by the thermal conductivity value at $T = 1500$ K. Materials marked with * have anisotropic thermal conductivity.

Compound	Thermal conductivity (HNEMD) (W/(m K))							
	300 K		1000 K		1500 K		2000 K	
	Quantum Corrected	Classical	Quantum Corrected	Classical	Quantum Corrected	Classical	Quantum Corrected	Classical
Sr ₂ AlNbO ₆	8.44 ± 0.19	9.50 ± 0.23	3.26 ± 0.12	3.31 ± 0.13	2.46 ± 0.11	2.48 ± 0.12	1.67 ± 0.10	1.68 ± 0.10
BaHfO ₃	9.28 ± 0.15	10.08 ± 0.18	3.09 ± 0.06	3.12 ± 0.64	2.38 ± 0.09	2.39 ± 0.09	1.84 ± 0.07	1.85 ± 0.07
Sr ₂ AlTaO ₆	9.21 ± 0.21	10.25 ± 0.23	3.32 ± 0.12	3.37 ± 0.13	2.26 ± 0.08	2.27 ± 0.12	1.70 ± 0.06	1.70 ± 0.06
SrTiO ₃	6.69 ± 0.15	7.72 ± 0.17	2.98 ± 0.11	3.03 ± 0.11	2.25 ± 0.09	2.26 ± 0.09	1.91 ± 0.06	1.91 ± 0.06
Sr ₂ AlNbO ₆ (disordered)	5.51 ± 0.16	6.28 ± 0.18	2.92 ± 0.11	2.97 ± 0.11	2.22 ± 0.08	2.23 ± 0.08	1.84 ± 0.07	1.84 ± 0.07
SrHfO ₃	2.74 ± 0.07	3.15 ± 0.09	2.14 ± 0.12	2.17 ± 0.11	1.85 ± 0.11	1.86 ± 0.11	1.64 ± 0.08	1.64 ± 0.08
Y ₂ Ti ₂ O ₇	2.38 ± 0.13	2.77 ± 0.15	1.88 ± 0.08	1.91 ± 0.08	1.76 ± 0.05	1.77 ± 0.05	1.54 ± 0.08	1.54 ± 0.08
CaZrO ₃	2.93 ± 0.13	3.34 ± 0.14	1.94 ± 0.08	1.96 ± 0.08	1.62 ± 0.09	1.63 ± 0.09	1.49 ± 0.08	1.49 ± 0.08
Gd ₃ Sc ₂ Al ₃ O ₁₂	3.97 ± 0.10	4.36 ± 0.10	1.86 ± 0.05	1.89 ± 0.05	1.58 ± 0.05	1.59 ± 0.05	1.35 ± 0.03	1.36 ± 0.03
Ca ₂ LaHf ₂ Al ₃ O ₁₂	2.93 ± 0.11	3.26 ± 0.11	1.99 ± 0.08	2.03 ± 0.08	1.50 ± 0.05	1.51 ± 0.05	1.50 ± 0.07	1.51 ± 0.07
SrBa ₂ MgTa ₂ O ₉ ^{a,b}	3.58 ± 0.10	3.91 ± 0.11	1.91 ± 0.06	1.93 ± 0.06	1.50 ± 0.07	1.51 ± 0.07	1.22 ± 0.07	1.23 ± 0.07
Ba ₃ MgTa ₂ O ₉ ^a	4.68 ± 0.16	5.07 ± 0.18	1.90 ± 0.11	1.92 ± 0.11	1.44 ± 0.10	1.45 ± 0.10	1.19 ± 0.10	1.20 ± 0.10
Ba ₃ YHfTaO ₉ ^{a,b}	3.32 ± 0.09	3.64 ± 0.10	1.77 ± 0.06	1.79 ± 0.06	1.44 ± 0.07	1.45 ± 0.07	1.24 ± 0.06	1.24 ± 0.06
SrBa ₂ MgNb ₂ O ₉ ^{a,b}	2.78 ± 0.13	3.11 ± 0.15	1.66 ± 0.08	1.69 ± 0.08	1.43 ± 0.08	1.44 ± 0.08	1.19 ± 0.07	1.19 ± 0.07
Gd ₂ Ti ₂ O ₇	2.13 ± 0.11	2.43 ± 0.13	1.58 ± 0.08	1.61 ± 0.08	1.41 ± 0.07	1.42 ± 0.07	1.38 ± 0.07	1.39 ± 0.07
La ₃ Lu ₂ Ga ₃ O ₁₂	5.22 ± 0.07	5.43 ± 0.07	1.89 ± 0.05	1.90 ± 0.05	1.40 ± 0.05	1.40 ± 0.05	0.98 ± 0.04	0.98 ± 0.04
Ba ₃ YZrTaO ₉ ^{a,b}	2.66 ± 0.11	2.92 ± 0.12	1.75 ± 0.07	1.77 ± 0.07	1.39 ± 0.09	1.40 ± 0.09	1.20 ± 0.07	1.20 ± 0.07
Ba ₃ YTiTaO ₉ ^{a,c}	3.32 ± 0.13	3.60 ± 0.14	1.55 ± 0.09	1.57 ± 0.09	1.37 ± 0.07	1.37 ± 0.07	1.12 ± 0.06	1.12 ± 0.06
Y ₂ AlTaO ₇ ^{a,b}	1.21 ± 0.07	1.46 ± 0.09	1.37 ± 0.12	1.40 ± 0.12	1.34 ± 0.09	1.35 ± 0.09	1.67 ± 0.11	1.68 ± 0.11
La ₃ Ca ₂ Nb ₃ O ₁₄ ^a	1.59 ± 0.06	1.83 ± 0.07	1.42 ± 0.07	1.44 ± 0.07	1.32 ± 0.04	1.33 ± 0.04	1.05 ± 0.05	1.06 ± 0.05
Ba ₃ YHfNbO ₉ ^{a,b}	2.59 ± 0.09	2.85 ± 0.11	1.67 ± 0.07	1.68 ± 0.07	1.31 ± 0.07	1.32 ± 0.07	1.15 ± 0.07	1.15 ± 0.07
Sr ₃ Y ₂ Ge ₃ O ₁₂	3.92 ± 0.12	4.18 ± 0.14	1.57 ± 0.04	1.59 ± 0.04	1.30 ± 0.08	1.30 ± 0.08	0.82 ± 0.09	0.82 ± 0.09
Ba ₃ YZrNbO ₉ ^{a,b}	2.34 ± 0.10	2.61 ± 0.11	1.69 ± 0.08	1.71 ± 0.08	1.30 ± 0.07	1.31 ± 0.07	1.19 ± 0.06	1.20 ± 0.06
La ₃ Mg ₂ Ta ₃ O ₁₄ ^{a,c}	1.87 ± 0.10	2.14 ± 0.10	1.40 ± 0.09	1.43 ± 0.09	1.27 ± 0.09	1.28 ± 0.09	1.18 ± 0.05	1.19 ± 0.05
La ₃ Mg ₂ Nb ₃ O ₁₄ ^{a,b}	1.77 ± 0.09	2.04 ± 0.10	1.48 ± 0.09	1.50 ± 0.09	1.27 ± 0.07	1.28 ± 0.07	1.05 ± 0.07	1.06 ± 0.07
La ₃ Ca ₂ Ta ₃ O ₁₄ ^{a,b}	1.71 ± 0.06	1.98 ± 0.07	1.46 ± 0.09	1.49 ± 0.09	1.24 ± 0.06	1.25 ± 0.06	1.08 ± 0.06	1.09 ± 0.06
Y ₃ Ca ₂ Nb ₃ O ₁₄ ^{a,b}	1.22 ± 0.07	1.45 ± 0.08	1.17 ± 0.09	1.20 ± 0.09	1.22 ± 0.09	1.23 ± 0.09	1.08 ± 0.05	1.08 ± 0.05
Gd ₂ AlTaO ₇ ^{a,c}	1.25 ± 0.09	1.49 ± 0.11	1.19 ± 0.08	1.22 ± 0.08	1.19 ± 0.09	1.21 ± 0.09
Gd ₂ Zr ₂ O ₇	1.21 ± 0.05	1.39 ± 0.04	1.16 ± 0.03	1.18 ± 0.03	1.19 ± 0.07	1.20 ± 0.07	1.03 ± 0.07	1.04 ± 0.07
Gd ₃ Ga ₅ O ₁₂	4.14 ± 0.14	4.36 ± 0.14	1.53 ± 0.09	1.55 ± 0.09	1.16 ± 0.08	1.16 ± 0.08	0.97 ± 0.11	0.97 ± 0.11
Ca ₃ Y ₂ Ge ₃ O ₁₂	2.61 ± 0.10	2.81 ± 0.12	1.29 ± 0.05	1.30 ± 0.05	1.16 ± 0.06	1.17 ± 0.06	1.04 ± 0.05	1.04 ± 0.05
La ₃ TaO ₇ ^a	1.69 ± 0.09	1.96 ± 0.09	1.24 ± 0.07	1.26 ± 0.07	1.08 ± 0.07	1.09 ± 0.07	0.97 ± 0.06	0.97 ± 0.06
Gd ₃ Sc ₂ Ga ₃ O ₁₂	0.76 ± 0.06	0.90 ± 0.07	0.99 ± 0.05	1.00 ± 0.05	1.00 ± 0.07	1.01 ± 0.07
Gd ₂ Hf ₂ O ₇	1.08 ± 0.06	1.24 ± 0.06	1.08 ± 0.05	1.09 ± 0.05	1.00 ± 0.05	1.00 ± 0.05	0.98 ± 0.06	0.99 ± 0.06

^aMaterials with the anisotropic structure.

^bHypothetical compounds.

^cKnown compound and hypothetical compounds.

02 March 2025 13:03:23

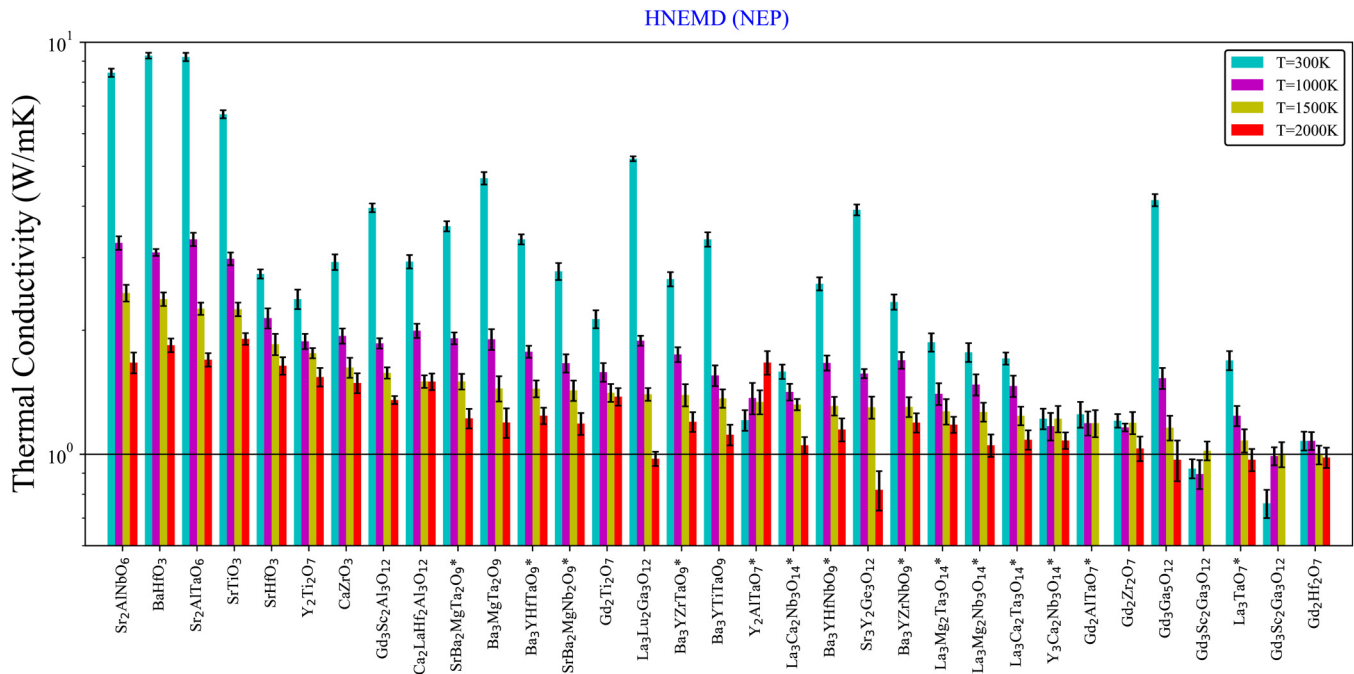


FIG. 2. Quantum-corrected thermal conductivity of the TBC material compounds calculated using the homogeneous nonequilibrium molecular dynamics approach (HNEMD) and machine-learning neuroevolution potential. The compounds are sorted by the thermal conductivity value at $T = 1500$ K. Materials marked with * have anisotropic thermal conductivity.

reduces the efficiency of heat transfer. Such reductions in thermal conductivity are advantageous in TBCs, as they enhance the material's ability to insulate underlying components from high temperatures, improving thermal resistance and prolonging the lifespan of components in high-temperature environments like gas turbines and aerospace engines.

We started by introducing on-site disorder into $\text{Sr}_2\text{AlNbO}_6$ and retraining the MTP and NEP potentials. To assess the effects of disorder, we calculated the thermal conductivity of disordered $\text{Sr}_2\text{AlNbO}_6$ over a wide temperature range from $T = 50$ K to $T = 2000$ K. The results, shown in Fig. 3, compare the thermal conductivity of ordered and disordered $\text{Sr}_2\text{AlNbO}_6$. As expected, disorder significantly reduces thermal conductivity at lower temperatures (below $T = 500$ K). However, at higher temperatures (above $T = 1000$ K), the difference between the thermal conductivities of ordered and disordered $\text{Sr}_2\text{AlNbO}_6$ becomes minimal and negligible. At high temperatures, intrinsic scattering dominates over extrinsic scattering caused by disorder. This is particularly important because thermal barrier coatings typically operate at temperatures around $T = 1200$ K and above.

We also considered the disorder effect on TEC on $\text{Sr}_2\text{AlNbO}_6$ and it was negligible. (see Fig. S5 in [supplementary material](#)).

D. Elastic constants and mechanical properties

Elastic properties and Pugh's ratio play a fundamental role in determining the mechanical integrity and thermal stability of TBCs.

These coatings are exposed to extreme conditions, including thermal cycling and mechanical loading, which require materials with strong mechanical properties. Elastic properties, such as Young's modulus E and Poisson's ratio ν , characterize a material's

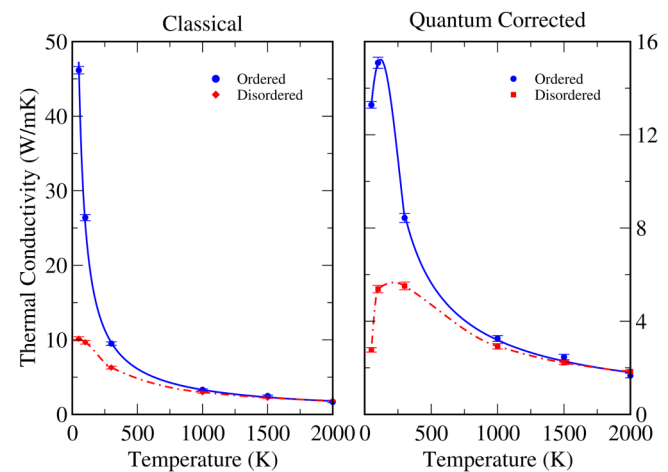


FIG. 3. Comparison thermal conductivity of order and disordered $\text{Sr}_2\text{AlNbO}_6$ from $T = 50$ K up to $T = 2000$ K.

ability to resist deformation under stress and maintain structural integrity. Pugh's ratio (G/K), which compares the bulk modulus K to the shear modulus G , provides insight into the brittleness or ductility of a material.

The fracture toughness of TBCs plays a crucial role in their ability to resist damage, delamination, and crack propagation under service conditions.⁵⁵ TBCs with low fracture toughness are particularly susceptible to delamination under erosion conditions. The fabricated YSZ TBCs have a toughness in the range of 0.1–0.5 MPa · m^{1/2} under service conditions.

The experimental measurement and theoretical estimation of fracture toughness are very complex. In this study, we used a recently proposed Mazhnik–Oganov model,⁵⁶

$$K_{IC} = \alpha_0^{-1/2} V_0^{1/6} [\zeta(v)E]^3/2, \quad (9)$$

where V_0 is the volume per atom, $\zeta(v)$ is a dimensionless function of Poisson's ratio, and $\alpha_0 = 8840$ GPa is a fitting parameter which depends on chemical bonding in the material and has units of pressure.

In our previous study,⁴ we demonstrated the capability of ML potentials in computing elastic properties, comparing them with DFT and experimental data. In this study, we utilized the elastic_vasp package,^{57,58} interfaced with MTP potentials. Bulk, Young's, and shear moduli, Pugh's ratio, and fracture toughness for each compound are shown in Table IV.

IV. SELECTING MATERIALS FOR THERMAL BARRIER COATINGS

We have set a threshold for thermal conductivity of 2 W/(mK) at $T = 1000$ K and a range of $(3.0-5.0) \times 10^{-5}$ K⁻¹ for average volumetric TEC from $T = 700$ K up to $T = 1300$ K in our material selection process for TBC applications, as illustrated in Fig. 4. Applying these criteria, we identified 16 compounds: CaZrO₃, Gd₃Sc₂Al₃O₁₂, Ba₃MgTa₂O₉, Gd₂Ti₂O₇, Ba₃YTiTaO₉, Gd₂Zr₂O₇, Gd₂Hf₂O₇, La₃Ca₂Nb₃O₁₄, La₃Mg₂Ta₃O₁₄, Gd₃Sc₂Ga₃O₁₂, Y₂Ti₂O₇, Sr₃Y₂Ge₃O₁₂, Gd₃Ga₅O₁₂, Ca₃Y₂Ge₃O₁₂, La₃TaO₇, and Gd₂AlTaO₇. This list could also include the hypothetical compounds SrBa₂MgTa₂O₉, SrBa₂MgNb₂O₉ (possible structural analogs of Ba₃MgTa₂O₉), La₃Mg₂Nb₃O₁₄ (an analog of La₃Ca₂Nb₃O₁₄), and Y₂AlTaO₇ with the proposed weberite structure. However, hypothetical compounds have not yet been obtained. The same applies to the known compounds Ba₃YTiTaO₉, La₃Mg₂Ta₃O₁₄, and Gd₂AlTaO₇ with the proposed structures.

Another important criterion for selecting TBCs is Pugh's ratio of less than 0.57, as shown in Fig. 5. Applying this criterion reduces the list to 14 compounds: CaZrO₃, Gd₃Sc₂Al₃O₁₂, Gd₂Ti₂O₇, Ba₃YTiTaO₉, Gd₂Zr₂O₇, Gd₂Hf₂O₇, SrBa₂MgNb₂O₉, La₃Ca₂Nb₃O₁₄, La₃Mg₂Ta₃O₁₄, La₃Mg₂Nb₃O₁₄, Gd₃Sc₂Ga₃O₁₂, Y₂Ti₂O₇, Sr₃Y₂Ge₃O₁₂, Gd₃Ga₅O₁₂, Ca₃Y₂Ge₃O₁₂, La₃TaO₇, and Gd₂AlTaO₇. Hypothetical compounds SrBa₂MgNb₂O₉ and La₃Mg₂Nb₃O₁₄ could be added in this row.

It is worth noting that Pugh's ratio for Ba₃MgTa₂O₉ is 0.62 and for SrBa₂MgTa₂O₉, it is 0.59, which is close to the border, so they are considered as potential candidates as well.

TABLE IV. Elastic properties: bulk modulus K , shear modulus G , Young's modulus E , Pugh's ratio, and fracture toughness K_{IC} of compounds calculated using MTP machine-learning potentials.

Compound	Elastic properties				
	K (GPa)	G (GPa)	E (GPa)	Pugh's ratio	K_{IC} (MPa m ^{1/2})
Sr ₂ AlNbO ₆	182.65	112.17	279.33	0.61	2.04
BaHfO ₃	173.08	106.39	264.90	0.61	1.87
Sr ₂ AlTaO ₆	185.75	117.56	291.25	0.63	2.09
SrTiO ₃	183.84	119.22	294.1	0.65	2.05
SrHfO ₃	170.39	96.78	244.12	0.57	1.78
Y ₂ Ti ₂ O ₇	209.23	103.82	267.25	0.49	2.27
CaZrO ₃	166.54	88.04	224.54	0.53	1.72
Gd ₃ Sc ₂ Al ₃ O ₁₂	154.03	78.98	202.36	0.51	1.44
Ca ₂ LaHf ₂ Al ₃ O ₁₂	144.77	79.58	201.76	0.55	1.37
SrBa ₂ MgTa ₂ O ₉ ^{a,b}	142.06	84.66	211.9	0.59	1.38
Ba ₃ MgTa ₂ O ₉ ^a	136.82	84.52	210.27	0.62	1.31
Ba ₃ YHfTaO ₉ ^{a,b}	152.63	89.83	225.3	0.59	1.53
SrBa ₂ MgNb ₂ O ₉ ^{a,b}	143.27	73.45	188.19	0.53	1.31
Gd ₂ Ti ₂ O ₇	173.86	87.66	225.14	0.50	1.69
La ₃ Lu ₂ Ga ₃ O ₁₂	148.31	65.53	171.36	0.44	1.32
Ba ₃ YZrTaO ₉ ^{a,b}	146.8	89.06	222.24	0.61	1.51
Ba ₃ YTiTaO ₉ ^{a,c}	139.68	74.96	190.76	0.54	1.29
Y ₂ AlTaO ₇ ^{a,b}	104.87	68.17	168.08	0.65	0.88
La ₃ Ca ₂ Nb ₃ O ₁₄ ^a	143.27	73.45	188.19	0.51	1.32
Ba ₃ YHfNbO ₉ ^{a,b}	157.71	92.62	232.36	0.59	1.61
Sr ₃ Y ₂ Ge ₃ O ₁₂	115.92	51.17	133.82	0.44	0.92
Ba ₃ YZrNbO ₉ ^{a,b}	142.79	84.32	211.35	0.59	1.40
La ₃ Mg ₂ Ta ₃ O ₁₄ ^{a,c}	159.55	86.11	218.94	0.54	1.56
La ₃ Mg ₂ Nb ₃ O ₁₄ ^{a,b}	155.08	77.82	200.01	0.50	1.49
La ₃ Ca ₂ Ta ₃ O ₁₄ ^{a,b}	158.04	86.51	219.48	0.55	1.58
Y ₃ Ca ₂ Nb ₃ O ₁₄ ^{a,b}	99.65	64.94	160.06	0.65	0.83
Gd ₂ AlTaO ₇ ^{a,c}	122.35	46.64	122.35	0.43	0.79
Gd ₂ Zr ₂ O ₇	164.47	81.98	210.9	0.50	1.64
Gd ₃ Ga ₅ O ₁₂	151.14	73.53	189.80	0.48	1.37
Ca ₃ Y ₂ Ge ₃ O ₁₂	114.80	49.88	130.71	0.43	0.88
La ₃ TaO ₇ ^a	130.08	65.85	169.03	0.50	1.13
Gd ₃ Sc ₂ Ga ₃ O ₁₂	111.36	48.23	126.44	0.43	0.84
Gd ₂ Hf ₂ O ₇	164.28	91.04	230.53	0.55	1.70

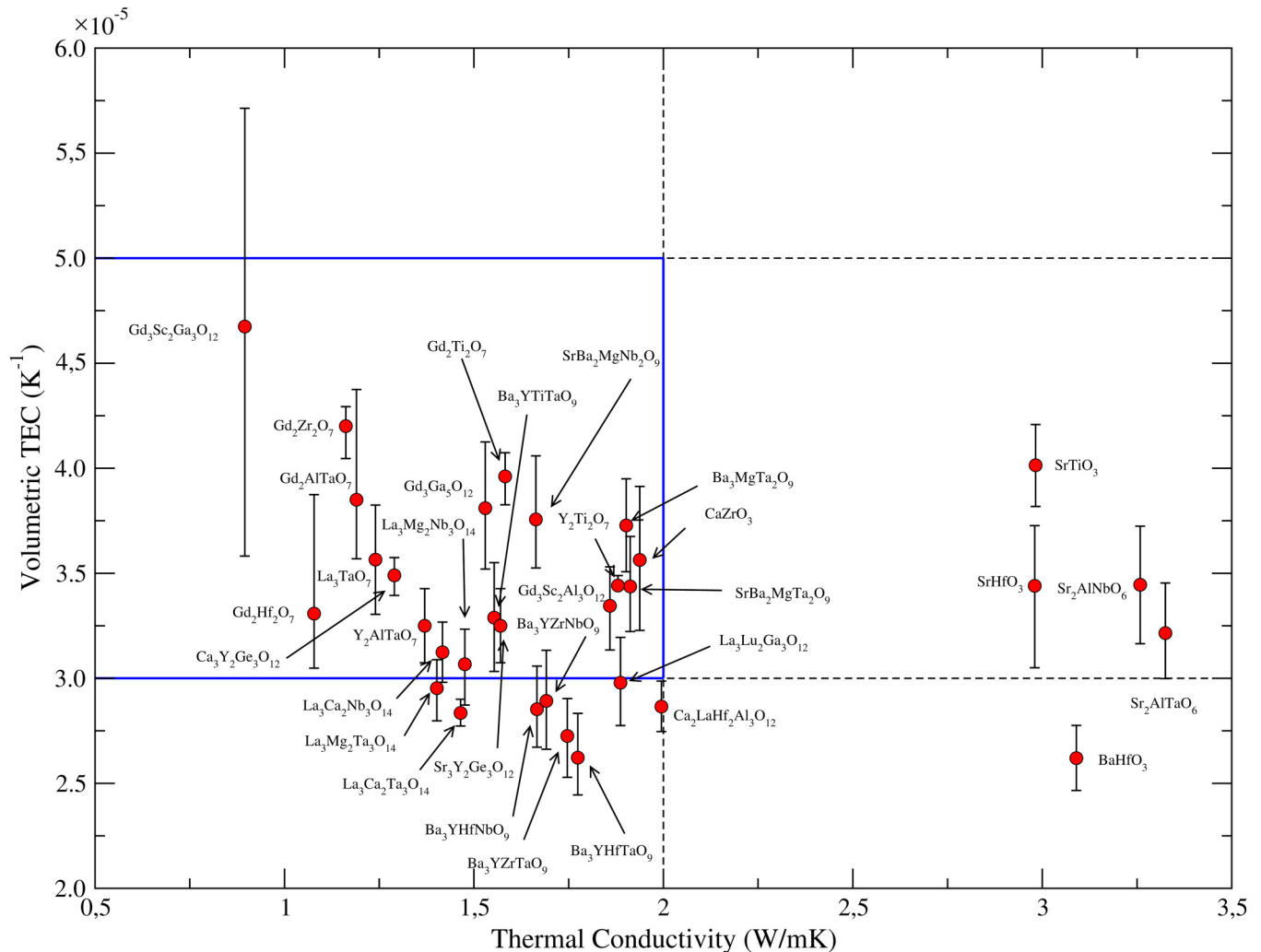
^aMaterials with the anisotropic structure.

^bHypothetical compounds.

^cKnown compound and hypothetical compounds.

Another important criterion for selecting TBCs is fracture toughness. Most candidates exhibit fracture toughness values higher than 1 MPa · m^{1/2}, (exception Gd₃Sc₂Ga₃O₁₂, Sr₃Y₂Ge₃O₁₂, Y₂AlTaO₇, Ca₃Y₂Ge₃O₁₂, and Gd₂AlTaO₇), i.e., they will likely have good resistance to erosion conditions.

The final list of selected materials from our previous work⁴ and the current study, along with their thermal conductivity (at $T = 1500$ K), volumetric TEC (at $T = 1500$ K), Pugh's ratio, and fracture toughness, is presented in Table V. These properties are compared with YSZ, the current dominant thermal barrier coating used in industry. It is clear that the thermophysical



02 March 2025 13:03:23

FIG. 4. Calculated thermal conductivity using HNEMD at $T = 1000$ K and the average quantum-corrected volumetric thermal expansion coefficient (PIMD) of candidate materials from $T = 700$ K up to $T = 1300$ K. Bars indicate the variation of TEC in this temperature range. The hypothetical compounds indicated with an asterisk (*).

properties of these compounds, primarily thermal conductivity, can be improved by introducing some isomorphous substitutions. It is worth noting that $\text{Ba}_3\text{MgTa}_2\text{O}_9$, $\text{Gd}_2\text{M}_2\text{O}_7$ ($M = \text{Ti}, \text{Zr}, \text{Hf}$), $\text{Y}_2\text{Ti}_2\text{O}_7$, La_3TaO_7 , and $\text{Gd}_2\text{AlTaO}_7$ are already considered as potential TBC materials, and $\text{Ba}_3\text{YTiTaO}_9$, $\text{La}_3\text{Ca}_2\text{Nb}_3\text{O}_{14}$, $\text{La}_3\text{Mg}_2\text{Ta}_3\text{O}_{14}$, $\text{Gd}_2\text{AlTaO}_7$, La_3TaO_7 , and $\text{Ba}_6\text{Ti}_2\text{Nb}_8\text{O}_{30}$ may have insufficient thermal stability or phase transitions preventing their use. Interestingly, our results on garnets prove to be unexpected, since they have not previously been considered as TBC materials. For these applications, other important characteristics of coatings should also be considered, for example, chemical stability and compatibility with bond coats, possible volatility of components, etc.

V. CONCLUSIONS

In conclusion, our study employed advanced computational techniques, including molecular dynamics simulations and machine-learning interatomic potentials, to investigate the thermal properties and mechanical characteristics of candidate TBC compounds. By employing these advanced computational techniques, we were able to obtain reliable estimates of thermal conductivity and thermal expansion coefficients for a range of temperatures, essential for understanding the behavior of TBC materials under different operating conditions.

In this study, we employed quantum corrections to estimate thermal conductivity using HNEMD and thermal expansion through PIMD, both of which are crucial at low temperatures.

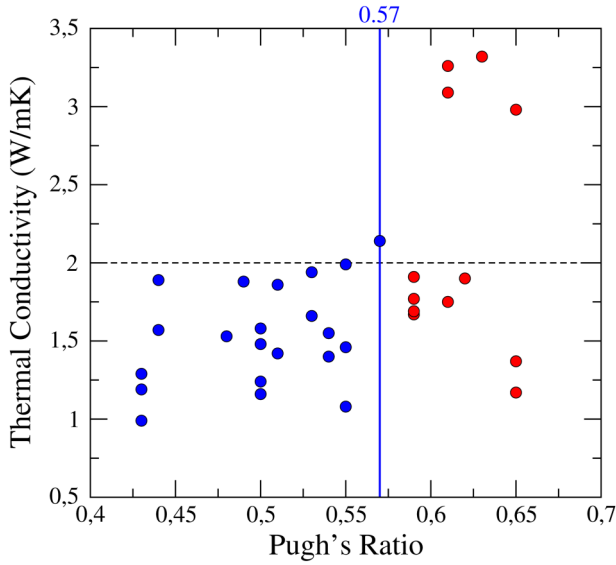


FIG. 5. Pugh's ratio of compounds with calculated thermal conductivity using HNEMD at $T = 1000$ K.

TABLE V. The thermal conductivity ($T = 1500$ K), volumetric thermal expansion ($T = 1500$ K), Pugh's ratio, and fracture toughness of selected materials for TBCs application.

Compound (structure)	Thermal conductivity (W/(m K))	TEC 10^{-5} (K^{-1})	Pugh's ratio	Fracture toughness ($MPa m^{1/2}$)
Perovskite				
CaZrO ₃ ^a (perovskite)	1.62 ± 0.09	4.16	0.53	1.72
SrBa ₂ MgNb ₂ O ₉ ^b (trigonal double perovskite)	1.43 ± 0.08	4.20	0.53	1.31
Ba ₃ YTiTaO ₉ ^c (trigonal double perovskite)	1.37 ± 0.07	3.80	0.54	1.29
Ba ₂ YNbO ₆ ^d (double perovskite)	1.36 ± 0.07	3.85	0.54	1.26
Ba ₂ YTaO ₆ ^d (double perovskite)	1.32 ± 0.08	3.50	0.57	1.27
Sr ₃ LaTa ₃ O ₁₂ ^d (layered perovskite)	1.10 ± 0.10	4.87	0.49	1.09
BaLaMgNbO ₆ ^d (double perovskite)	1.14 ± 0.09	5.40	0.48	0.75
BaLaMgTaO ₆ ^d (double perovskite)	1.11 ± 0.10	5.16	0.26	1.61
Ba ₃ LaTa ₃ O ₁₂ ^d (layered perovskite)	0.84 ± 0.09	3.10	0.57	1.08
Garnet				
Gd ₃ Sc ₃ Al ₃ O ₁₂ (garnet)	1.58 ± 0.05	3.69	0.51	1.44
	1.41 ± 0.05	3.66	0.50	1.21

TABLE V. (Continued.)

Compound (structure)	Thermal conductivity (W/(m K))	TEC 10^{-5} (K^{-1})	Pugh's ratio	Fracture toughness ($MPa m^{1/2}$)
Ca ₂ YZr ₂ Al ₃ O ₁₂ ^d (garnet)				
Sr ₃ Y ₂ Ge ₃ O ₁₂ (garnet)	1.30 ± 0.08	3.58	0.44	0.92
Gd ₃ Ga ₅ O ₁₂ (garnet)	1.16 ± 0.08	4.43	0.48	1.37
Ca ₃ Y ₂ Ge ₃ O ₁₂ (garnet)	1.16 ± 0.06	3.68	0.43	0.88
Gd ₃ Sc ₂ Ga ₃ O ₁₂ (garnet)	1.00 ± 0.07	7.29	0.43	0.84
Pyrochlore				
Y ₂ Ti ₂ O ₇ (cubic pyrochlore)	1.76 ± 0.05	3.56	0.49	2.27
Gd ₂ Ti ₂ O ₇ (cubic pyrochlore)	1.41 ± 0.07	4.27	0.50	1.69
La ₃ Mg ₂ Ta ₃ O ₁₄ ^c (trigonal ordered pyrochlore)	1.32 ± 0.04	3.15	0.54	1.56
La ₃ Mg ₂ Nb ₃ O ₁₄ ^b (trigonal ordered pyrochlore)	1.27 ± 0.07	3.35	0.50	1.49
La ₃ Ca ₂ Nb ₃ O ₁₄ (trigonal ordered pyrochlore)	1.24 ± 0.06	3.40	0.51	1.32
Gd ₂ Zr ₂ O ₇ (cubic pyrochlore)	1.19 ± 0.07	3.98	0.50	1.64
Gd ₂ Hf ₂ O ₇ (cubic pyrochlore)	1.00 ± 0.05	3.05	0.55	1.70
Others				
CaLaAl ₃ O ₇ ^d (melilite)	1.46 ± 0.16	3.25	0.47	1.03
Ba ₆ Ti ₂ Nb ₈ O ₃₀ ^d (tetragonal tungsten bronze)	1.12 ± 0.10	5.43	0.46	0.85
Y ₄ Ca(SiO ₄) ₃ O ^d (apatite)	1.04 ± 0.05	4.02	0.43	0.88
Gd ₂ AlTaO ₇ ^d (weberite)	1.19 ± 0.09	4.69	0.43	0.79
La ₃ TaO ₇ (distorted weberite)	1.08 ± 0.07	4.11	0.50	1.13
8% YSZ (exp. at $T = 1000$ K)	~2.0 ⁵⁹	~3.21 ⁶⁰	...	1.49 ⁶¹
8% YSZ (theor. at $T = 1000$ K) ⁴	2.24 ± 0.13	4.06		
10% YSZ <100> (exp.) ⁶²				1.9 ± 0.1
10% YSZ <110> (exp.) ⁶²				1.1 ± 0.1

^aHas phase transition to cubic perovskite at 2023 K.

^bHypothetical compounds.

^cKnown compounds and hypothetical compounds.

^dMaterials identified in our paper.⁴

Another important phenomenon we investigated in thermal conductivity in TBCs is the effect of disorder. Our study revealed that disorder has a strong impact at low temperatures, but at high temperatures (above $T = 1000$ K), the influence of disorder diminishes, causing the thermal conductivity of disordered materials to approach that of perfect crystals. This finding is particularly important because the operating temperatures of TBCs are typically near or exceed $T = 1200$ K.

Furthermore, our study identified promising TBC materials based on specific criteria such as thermal conductivity, thermal expansion coefficients, and mechanical properties. By considering these criteria, we narrowed down the list of potential TBC materials to a select few, which exhibit desirable thermal and mechanical properties for high-temperature applications.

Overall, our research contributes to the ongoing efforts in materials science and engineering to develop improved TBC materials. Further experimental validation of the identified materials will be crucial for their eventual deployment in practical applications, paving the way for more efficient and reliable thermal barrier coatings in the future.

SUPPLEMENTARY MATERIAL

Supplementary material includes additional information about (a) comparing the calculated thermal expansion coefficient and thermal conductivity of compounds with available experimental data at the same temperatures. (b) Phase transition of SrHfO_3 and CaZrO_3 from $T = 100$ K to $T = 2200$ K. (c) Thermal expansion coefficient of ordered and disordered $\text{Sr}_2\text{AlNbO}_6$ from $T = 150$ K to $T = 2000$ K.

ACKNOWLEDGMENTS

We acknowledge the Russian Science Foundation (Grant No. 23-13-00117) for supporting HNEMD results and Grant No. 19-72-30043 for supporting TEC calculation. GPU computations were performed on the High-Performance Computing (HPC) system Zhores at Skolkovo Institute of Science and Technology.⁶³

AUTHOR DECLARATIONS

Conflict of Interest

The authors have no conflicts to disclose.

Author Contributions

Majid Zeraati: Conceptualization (equal); Data curation (equal); Investigation (equal); Methodology (equal); Software (equal); Visualization (equal); Writing – original draft (equal); Writing – review & editing (equal). **Artem R. Oganov:** Conceptualization (equal); Methodology (equal); Supervision (equal); Writing – original draft (equal); Writing – review & editing (equal). **Alexey P. Maltsev:** Data curation (equal); Software (supporting). **Sergey F. Solodovnikov:** Conceptualization (equal); Supervision (equal); Writing – original draft (equal); Writing – review & editing (equal).

DATA AVAILABILITY

The data that support the findings of this study available from the corresponding author upon reasonable request.

REFERENCES

1. L. Huang, H. M. Meng, J. Tang, S. Li, and Z. Q. Yu, *Adv. Mater. Res.* **1053**, 364 (2014).
2. R. Vaßen, E. Bakan, D. E. Mack, and O. Guillon, *J. Therm. Spray Tech.* **31**, 685 (2022).
3. B. Liu, Y. Liu, C. Zhu, H. Xiang, H. Chen, L. Sun, Y. Gao, and Y. Zhou, *J. Mater. Sci. Technol.* **35**, 833 (2019).
4. M. Zeraati, A. R. Oganov, T. Fan, and S. F. Solodovnikov, *Phys. Rev. Mater.* **8**, 033601 (2024).
5. G. C. Sosso, D. Donadio, S. Caravati, J. Behler, and M. Bernasconi, *Phys. Rev. B* **86**, 104301 (2012).
6. H. Babaei, R. Guo, A. Hashemi, and S. Lee, *Phys. Rev. Mater.* **3**, 074603 (2019).
7. P. Korotaev, I. Novoselov, A. Yanilkin, and A. Shapeev, *Phys. Rev. B* **100**, 144308 (2019).
8. J. Brorsson, A. Hashemi, Z. Fan, E. Fransson, F. Eriksson, T. Ala-Nissila, A. V. Krasheninnikov, H. Komsa, and P. Erhart, *Adv. Theory Simul.* **5**, 2100217 (2022).
9. G. Kresse and J. Furthmüller, *Phys. Rev. B* **54**, 11169 (1996).
10. P. E. Blöchl, *Phys. Rev. B* **50**, 17953 (1994).
11. J. P. Perdew, A. Ruzsinszky, G. I. Csonka, O. A. Vydrov, G. E. Scuseria, L. A. Constantin, X. Zhou, and K. Burke, *Phys. Rev. Lett.* **100**, 136406 (2008).
12. J. P. Perdew, K. Burke, and M. Ernzerhof, *Phys. Rev. Lett.* **77**, 3865 (1996).
13. H. J. Monkhorst and J. D. Pack, *Phys. Rev. B* **13**, 5188 (1976).
14. M. Parrinello and A. Rahman, *Phys. Rev. Lett.* **45**, 1196 (1980).
15. M. Parrinello and A. Rahman, *J. Appl. Phys.* **52**, 7182 (1981).
16. A. V. Shapeev, *Multiscale Model. Simul.* **14**, 1153 (2016).
17. E. V. Podryabinkin and A. V. Shapeev, *Comput. Mater. Sci.* **140**, 171 (2017).
18. K. Gubaev, E. V. Podryabinkin, G. L. Hart, and A. V. Shapeev, *Comput. Mater. Sci.* **156**, 148 (2019).
19. Y. Zuo, C. Chen, X. Li, Z. Deng, Y. Chen, J. Behler, G. Csányi, A. V. Shapeev, A. P. Thompson, M. A. Wood, and S. P. Ong, *J. Phys. Chem. A* **124**, 731 (2020).
20. I. S. Novikov, K. Gubaev, E. V. Podryabinkin, and A. V. Shapeev, *Mach. Learn. Sci. Technol.* **2**, 025002 (2021).
21. A. P. Thompson, H. M. Aktulga, R. Berger, D. S. Bolintineanu, W. M. Brown, P. S. Crozier, P. J. in 't Veld, A. Kohlmeyer, S. G. Moore, T. D. Nguyen, R. Shan, M. J. Stevens, J. Tranchida, C. Trott, and S. J. Plimpton, *Comput. Phys. Commun.* **271**, 108171 (2022).
22. Z. Fan, Z. Zeng, C. Zhang, Y. Wang, K. Song, H. Dong, Y. Chen, and T. Ala-Nissila, *Phys. Rev. B* **104**, 104309 (2021).
23. Z. Fan, *J. Phys.: Condens. Matter* **34**, 125902 (2022).
24. Z. Fan, Y. Wang, P. Ying, K. Song, J. Wang, Y. Wang, Z. Zeng, K. Xu, E. Lindgren, J. M. Rahm, A. J. Gabourie, J. Liu, H. Dong, J. Wu, Y. Chen, Z. Zhong, J. Sun, P. Erhart, Y. Su, and T. Ala-Nissila, *J. Chem. Phys.* **157**, 114801 (2022).
25. K. Song, R. Zhao, J. Liu, Y. Wang, E. Lindgren, Y. Wang, S. Chen, K. Xu, T. Liang, P. Ying, N. Xu, Z. Zhao, J. Shi, J. Wang, S. Lyu, Z. Zeng, S. Liang, H. Dong, L. Sun, Y. Chen, Z. Zhang, W. Guo, P. Qian, J. Sun, P. Erhart, T. Ala-Nissila, Y. Su, and Z. Fan, *Nat. Commun.* **15**, 10208 (2024).
26. Z. Fan, W. Chen, V. Vierimaa, and A. Harju, *Comput. Phys. Commun.* **218**, 10 (2017).
27. C. Y. Ho and R. E. Taylor, *Thermal Expansion of Solids* (ASM International, 1998), Vol. 4.
28. D. Wallace, *Thermodynamics of Crystals* (Wiley, 1972).
29. P. Carrier, R. Wentzcovitch, and J. Tsuchiya, *Phys. Rev. B* **76**, 064116 (2007).
30. M. Ceriotti, M. Parrinello, T. E. Markland, and D. E. Manolopoulos, *J. Chem. Phys.* **133**, 124104 (2010).

- ³¹R. P. Feynman and A. R. Hibbs, *The Path Integral Formulation of Quantum Mechanics* (McGraw-Hill, New York, 1965).
- ³²M. Parrinello and A. Rahman, *J. Chem. Phys.* **80**, 860 (1984).
- ³³P. Ying, W. Zhou, L. Svensson, E. Berger, E. Fransson, F. Eriksson, K. Xu, T. Liang, J. Xu, B. Song, S. Chen, P. Erhart, and Z. Fan, arxiv.org/abs/2409.04430 (2024).
- ³⁴J. Yang, C. Wan, M. Zhao, M. Shahid, and W. Pan, *J. Eur. Ceram. Soc.* **36**, 3809 (2016).
- ³⁵Z. Tian, L. Zheng, J. Wang, P. Wan, J. Li, and J. Wang, *J. Eur. Ceram. Soc.* **36**, 189 (2016).
- ³⁶L. Chen, M. Hu, J. Guo, X. Chong, and J. Feng, *J. Mater. Sci. Technol.* **52**, 20 (2020).
- ³⁷R. Peierls, *Ann. Phys.* **395**, 1055 (1929).
- ³⁸M. Omini and A. Sparavigna, *Phys. B* **212**, 101 (1995).
- ³⁹M. Omini and A. Sparavigna, *Phys. Rev. B* **53**, 9064 (1996).
- ⁴⁰P. Souvatzis, O. Eriksson, M. I. Katsnelson, and S. P. Rudin, *Phys. Rev. Lett.* **100**, 095901 (2008).
- ⁴¹O. Hellman, I. A. Abrikosov, and S. I. Simak, *Phys. Rev. B* **84**, 180301(R) (2011).
- ⁴²F. Eriksson, E. Fransson, and P. Erhart, *Adv. Theory Simul.* **2**, 1800184 (2019).
- ⁴³D. J. Evans, *Phys. Lett. A* **91**, 457 (1982).
- ⁴⁴D. J. Evans and B. L. Holian, *J. Chem. Phys.* **83**, 4069 (1985).
- ⁴⁵Z. Fan, H. Dong, A. Harju, and T. Ala-Nissila, *Phys. Rev. B* **99**, 064308 (2019).
- ⁴⁶K. Sääskilähti, J. Oksanen, J. Tulkki, A. McGaughey, and S. Volz, *AIP Adv.* **6**, 121904 (2016).
- ⁴⁷Y. Wang, Z. Fan, P. Qian, M. A. Caro, and T. Ala-Nissila, *Phys. Rev. B* **107**, 054303 (2023).
- ⁴⁸T. Liang, P. Ying, K. Xu, Z. Ye, C. Ling, Z. Fan, and J. Xu, *Phys. Rev. B* **108**, 184203 (2023).
- ⁴⁹K. Xu, Y. Hao, T. Liang, P. Ying, J. Xu, J. Wu, and Z. Fan, *J. Chem. Phys.* **158**, 204114 (2023).
- ⁵⁰J. F. Nye *et al.*, *Physical Properties of Crystals: Their Representation by Tensors and Matrices* (Oxford University Press, 1985).
- ⁵¹L. Wang, J. D. Lee, and C.-D. Kan, *Int. J. Smart Nano Mater.* **7**, 144 (2016).
- ⁵²W. Voigt, *Lehrbuch der Kristallphysik (mit ausschluß der kristalloptik)* (B.G. Teubner, Leipzig, 1910, 1928).
- ⁵³A. Reuss, *Z. Angew. Math. Mech.* **9**, 49 (1929).
- ⁵⁴R. Hill, *Proc. Phys. Soc. A* **65**, 349 (1952).
- ⁵⁵X. Geng, R. Wellman, L. I. Arrom, C. Chalk, and G. M. Castelluccio, *Ceram. Int.* **49**, 25788 (2023).
- ⁵⁶E. Mazhnik and A. R. Oganov, *J. Appl. Phys.* **126**, 125109 (2019).
- ⁵⁷P. Kumar and I. Adlakha, *J. Eng. Mater. Technol.* **145**, 011003 (2023).
- ⁵⁸P. Mishra, P. Kumar, L. Neelakantan, and I. Adlakha, *Comput. Mater. Sci.* **214**, 111667 (2022).
- ⁵⁹K. W. Schlichting, N. P. Pature, and P. G. Klemens, *J. Mater. Sci.* **36**, 3003 (2001).
- ⁶⁰R. Vaßen, G. Kerkhoff, and D. Stöver, *Mater. Sci. Eng. A* **303**, 100 (2001).
- ⁶¹Y. Li, H. Sun, J. Song, Z. Zhang, H. Lan, L. Tian, and K. Xie, *Materials* **16**, 2019 (2023).
- ⁶²A. Pajares, F. Guiberteau, A. Dominguez-Rodriguez, and A. H. Heuer, *J. Am. Ceram. Soc.* **71**, C-332 (1988).
- ⁶³I. Zacharov, R. Arslanov, M. Gunin, D. Stefonishin, A. Bykov, S. Pavlov, O. Panarin, A. Maliutin, S. Rykovanov, and M. Fedorov, *Open Eng.* **9**, 512 (2019).